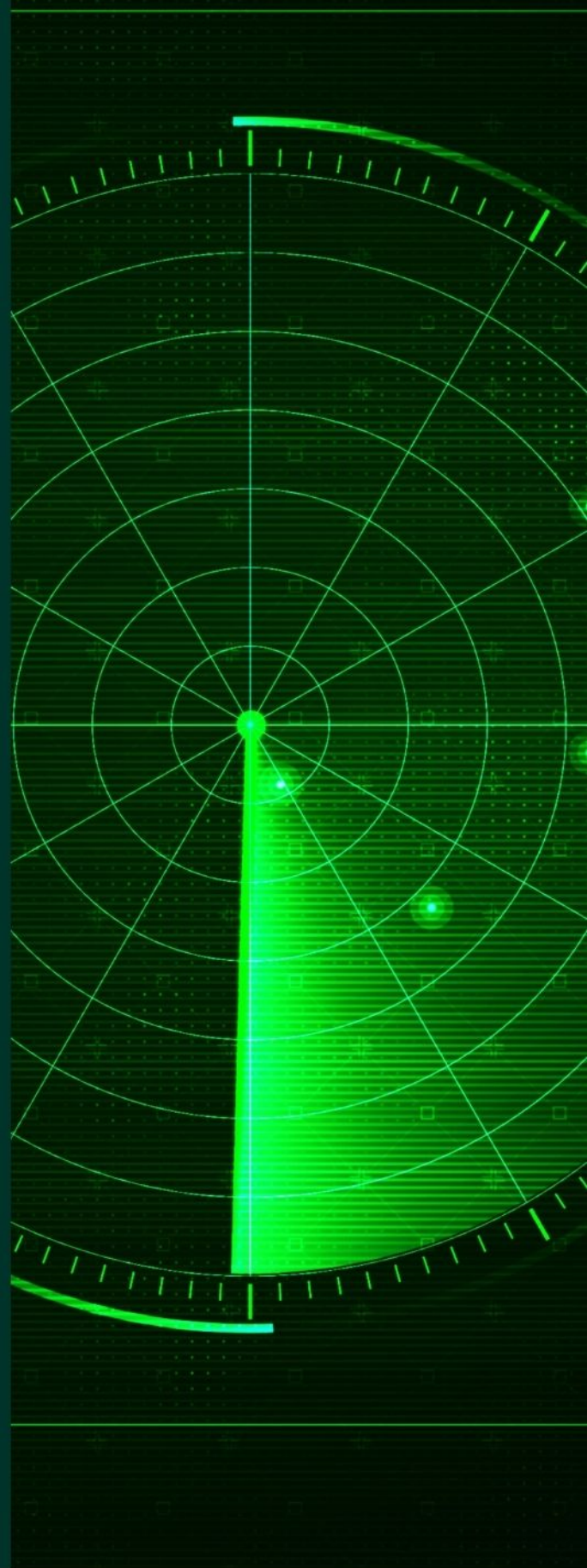# IET Radar, Sonar & Navigation

Special Issue Call for Papers

**Be Seen. Be Cited.
Submit your work to a new IET special issue**

Connect with researchers and experts in your field and share knowledge.

Be part of the latest research trends, faster.

Read more

IET The Institution of Engineering and Technology

IET Radar, Sonar & Navigation

ORIGINAL RESEARCH

Advanced direction of arrival estimation using step-learnt iterative soft-thresholding for frequency-modulated continuous wave multiple-input multiple-output radar

Seongmin Hong[1]　|　Seong-Cheol Kim[1]　|　Seongwook Lee[2] 🆔

[1]Department of Electrical and Computer Engineering and Institute of New Media & Communications (INMC), Seoul National University (SNU), Seoul, Republic of Korea

[2]School of Electronics and Information Engineering, Korea Aerospace University, Goyang-si, Gyeonggi-do, Republic of Korea

Correspondence

Seongwook Lee, School of Electronics and Information Engineering, Korea Aerospace University, 76, Hanggongdaehak-ro, Deogyang-gu, Goyang-si, Gyeonggi-do, Republic of Korea.
Email: swl90@kau.ac.kr

Abstract

The number of antennas in automotive frequency-modulated continuous wave (FMCW) multiple-input multiple-output (MIMO) radar systems is increasing. Existing greedy or subspace-based methods cannot quickly and accurately estimate the direction of arrival (DoA) of the target. Therefore, we propose a fast and accurate DoA estimation algorithm for the automotive FMCW MIMO radar. To achieve both fastness and accuracy, we exploit the group sparsity in DoA estimation by defining the problem as a multiple measurement vector (MMV) compressive sensing and extend the step-learnt iterative soft-thresholding algorithm (SLISTA) to the MMV problem. To apply the extended SLISTA, we train the network in an unsupervised manner and normalise the input. We conduct experiments to evaluate the performance of the proposed method. Compared to the algorithms such as ISTA/FISTA/MFOCUSS that solve the same optimisation problem, the extended SLISTA exhibits the most accurate DoA estimation results for actual targets, with less execution time than a subspace-based method. Moreover, the results show that the extended SLISTA prevents false detections, whereas greedy and subspace-based methods do not.

1 | INTRODUCTION

Radar has emerged as a critical technology for autonomous driving. Unlike other automotive sensors, such as cameras and lidars, radars have a unique advantage that their performance does not deteriorate despite the changes in weather and light conditions [1]. Fast-chirp frequency modulated continuous wave (FMCW) radar using the 77–81 GHz frequency band is widely used for automotive due to its high range resolution and low cost [2]. One crucial challenge of the fast-chirp FMCW radar is achieving a high angular resolution [3]. To this end, the number of antennas must be increased. Many researchers have used multiple-input multiple-output (MIMO) radar [4] to maximise the number of antennas, even with a limited radar form factor. The number of antennas (i.e., the number of virtual array elements) of the MIMO radar is obtained by multiplying the number of transmit and receive antennas [5]. In the past, the fast-chirp FMCW MIMO radars used about 10 antennas at most [6–10]; however, MIMO radars with more than a hundred antennas [11] are being released.

MIMO radar with many antennas requires a much heavier computational burden for direction-of-arrival (DoA) estimation. This computational burden can prevent cars equipped with FMCW MIMO radars from making real-time decisions on the road. The angle fast Fourier transform (angle-FFT), defined as a single matrix product, has the lowest computational complexity among the DoA estimation algorithms. In FMCW MIMO radars with few antennas, the angle-FFT has been mainly used as a preprocessing algorithm for high-level signal processing such as target classification through artificial neural networks [12–14]. However, because the angle-FFT shows low performance among DoA estimation algorithms due to the low angular resolution and high sidelobe level [15], many studies use more accurate DoA estimation algorithms with higher computational complexity. Subspace-based methods, such as the multiple signal classification (MUSIC) [16] and the estimation of signal parameters via rotational invariant techniques (ESPRIT) [17–20], have been widely used in conventional MIMO radars because they can obtain higher angular resolution than the angle-FFT. However, in the latest

MIMO radar with a large number of antennas, we cannot obtain both estimation accuracy and computational speed simultaneously with existing subspace-based DoA estimation algorithms. Because subspace-based methods require floating-point operations proportional to the third power of antennas [21], an excessive computational burden can be incurred when the number of antennas becomes large. Therefore, we aim to find DoA estimation algorithms that are more accurate than the angle-FFT and faster than subspace-based methods.

Compressive sensing (CS) is an appropriate approach for fast and accurate DoA estimation. CS is a technique for recovering sparse vectors. Because FMCW MIMO radar's DoA estimation has sparsity (i.e., reflected signals come from only a few directions in the field of view (FoV)), many studies have achieved good performance using CS [22–24]. The CS problem is divided into a single measurement vector (SMV) problem and a multiple measurement vector (MMV) problem. The SMV problem reconstructs one vector, whereas the MMV problem reconstructs multiple vectors simultaneously. For the CS problem to be defined as the MMV problem, the vectors to be reconstructed must have joint sparsity. The joint sparsity refers to the property that sparse vectors have similar nonzero indices. Due to the high range resolution, FMCW MIMO radar signals with similar ranges and velocities have similar DoAs, meaning they have joint sparsity. Therefore, the DoA estimation problem in the FMCW MIMO radar should be formulated as an MMV problem to exploit the joint sparsity. Some studies [22, 25–27] formulated the DoA estimation problem of the MIMO radar as an MMV problem.

However, the studies defining the DoA estimation in FMCW MIMO radar as an MMV problem have not successfully answered the following question: Are proposed methods faster than subspace-based methods and more accurate than the angle-FFT for actual data? In particular, many studies have used iterative algorithms, which have made it challenging to satisfy fastness. Recently, many studies have realised fast imaging in magnetic resonance imaging (MRI) and vision image reconstruction by treating CS algorithms as a learnable recurrent neural network. This technique is referred to as algorithm unrolling [28]. The step-learnt iterative soft-thresholding algorithm (SLISTA) [29] is an application of algorithm unrolling for the iterative soft-thresholding algorithm (ISTA) [30]. Unlike other unrolled ISTAs, unsupervised learning is possible in SLISTA. That is, it is possible to learn the network for actual radar data whose ground truth is unknown. However, SLISTA solves the lasso, a type of SMV problem. Therefore, we extend SLISTA to the MMV problem and train it in an unsupervised manner. To this end, we set the group lasso [31], the MMV version of the lasso, as the objective function, and train the network (i.e., SLISTA) in an unsupervised manner. We also normalise the input before applying the algorithm for the robust DoA estimation.

To evaluate the performance of DoA estimation algorithms, we conduct measurement experiments using a fast-chirp FMCW MIMO radar in the test field. Through the experiments, we measure the execution time of the algorithms and compare the estimation results. In addition, we compare how sharp the imaged target (i.e., corner reflector) appears. We verify that the proposed method satisfies both fastness and accuracy via the measurements.

In summary, the major contributions of this study are as follows:

- We extend SLISTA to the MMV problem for the DoA estimation in the fast-chirp FMCW MIMO radar.
- We train the network and propose a normalisation process to apply the extended SLISTA.
- We experimentally verify that the proposed method exhibits better imaging results than the other algorithms in a shorter computation time than MUSIC.

The remainder of this study is organised as follows. The distance, velocity, and DoA estimation methods in the FMCW MIMO radar system are introduced in Section 2. In Section 3, we explain the interpretation of the DoA estimation problem as a CS problem. A fast CS-based DoA estimation method is proposed in Section 4. The performance of the proposed method is verified through actual experiments in Section 5. Finally, we present our conclusion in Section 6.

The following symbols will be used throughout the study:

- x, x, $\mathbf{X}$ represent a scalar, vector, and matrix, respectively.
- For $p \in [0, \infty]$, $\|\cdot\|_p$ is the l_p norm.
- The Frobenius matrix norm is $\|\cdot\|_F$.
- The identity matrix of size m is $\mathbf{I}_{m \times m}$.
- The pseudoinverse of a matrix $\mathbf{X}$ is $\mathbf{X}^\dagger$.
- Subscript x_k denotes the kth element of x.
- Superscript $\mathrm{x}^{(p)}$ represents x at iteration p.
- The kth row of $\mathbf{X}$ is $\mathbf{X}_{[k,:]}$.
- kth column of $\mathbf{X}$ is $\mathbf{X}_{[:,k]}$.
- Superscript $(\cdot)^H$ denotes the Hermitian operator.
- The support of $\mathbf{X}$, supp($\mathbf{X}$) denotes the index set corresponding to nonzero rows.
- The notation $\otimes$ denotes the Kronecker product.

2 | FUNDAMENTALS OF FMCW MIMO RADAR SYSTEMS

2.1 | Range and velocity estimation

We begin by explaining how the range and velocity are estimated in a fast-chirp FMCW radar. The mth chirp of the transmitted signal can be expressed as

$$T(m, t) = A_T \exp\left[j2\pi\left\{\left(f_c - \frac{B}{2}\right)t + \frac{S}{2}t^2\right\}\right]$$
$$\text{rect}\left(\frac{t - m\Delta T_c}{\Delta T_{sw}} - \frac{1}{2}\right), \tag{1}$$

where B is the sweep bandwidth, ΔT_c is the transmission period of each chirp, and ΔT_{sw} is the sweep duration, as shown in Figure 1. In addition, A_T, $S = \frac{B}{\Delta T_{sw}}$, f_c represents the amplitude of the transmitted signal, sweep slope, and carrier frequency, respectively. The notation rect($\cdot$) denotes the rectangular pulse function, which is defined as follows:

$$\text{rect}(u) = \begin{cases} 1, & \text{if } -1/2 < u < 1/2 \\ 0, & \text{otherwise.} \end{cases} \quad (2)$$

When the signal in Figure 1 is radiated through the transmit antenna, the FMCW radar receives the reflected signal from the target. Suppose the target has a distance r and a relative radial velocity v from the radar system. Then the received signal will have a time delay of $t_d = \frac{2(r + mv\Delta T_c)}{c}$ and a Doppler shift of $f_D = \frac{2vf_c}{c}$. The received signal is expressed as

$$R(m, t) = A_R \exp\left[j2\pi\left\{\left(f_c - \frac{B}{2} + f_D\right)(t - t_d)\right.\right.$$
$$\left.\left. + \frac{S}{2}(t - t_d)^2\right\}\right]\text{rect}\left(\frac{t - m\Delta T_c}{\Delta T_{sw}} - \frac{1}{2}\right), \quad (3)$$

where A_R is the amplitude of the received signal.

We obtain the baseband signal after mixing the transmitted and received signals. The baseband signal is expressed as

$$b(m, t) = \text{LPF}(T^*(m, t)R(m, t))$$
$$= \frac{1}{2}A_T A_R \exp\left[j2\pi\left(\frac{2f_c(r + mv\Delta T_{sw})}{c}\right.\right.$$
$$\left.\left. + \frac{2BR}{c\Delta T_{sw}}t\right)\right]\text{rect}\left(\frac{t - m\Delta T_c}{\Delta T_{sw}} - \frac{1}{2}\right), \quad (4)$$

where LPF($\cdot$) denotes a low-pass filter. Note that $b(m, t)$ has the same frequency as the beat frequency (i.e., frequency difference) between $T(m, t)$ and $R(m, t)$. In (4), $b(m, t)$ has a frequency of $\frac{2Br}{c\Delta T_{sw}}$, and a phase of $2\pi\frac{2f_c(r + mv\Delta T_{sw})}{c}$. The frequency is proportional to r, and the phase is proportional to v when r is fixed. Thus, to extract the range and velocity information of the target from $b(m, t)$, we apply the Fourier transforms with respect to t and m, respectively. First, $b(m, t)$ is converted to a discrete-time signal $b[m, n] = b(m, n\Delta T_s)$ by an analogue-to-digital converter (ADC), where ΔT_s represents the sampling period. Then, the FFT is applied to $b[m, n]$ to extract the range and velocity of the target.

As shown in Figure 1, two FFTs are applied sequentially to the ADC data. We first obtain the range spectrum by applying FFT with respect to n. Subsequently, we obtain the velocity spectrum by applying FFT with respect to the chirp index m. These FFTs are called range-FFT and velocity-FFT, respectively. Through these FFTs, we can obtain the range-velocity map containing the range and velocity information of the targets [32]. On the range-velocity map, the range and velocity bin sizes are calculated as $\Delta r = c/2S\Delta T_s N_{ADC}$ and $\Delta v = c/2f_c\Delta T_c M_T N_c$, respectively, where c is the speed of light, N_{ADC} is the number of ADC data in one chirp, N_C is the number of chirps, and M_T is the number of transmit antennas.

2.2 | DoA estimation

This section describes the DoA estimation performed on this range-velocity map. The higher the number of antennas, the better the DoA estimation performance. However, having a large number of antennas requires a large radar aperture. MIMO radars using multiple transmit/receive antennas exhibit good DoA estimation performance, even with a small aperture. In our study, we consider a fast-chirp FMCW MIMO radar with M_T transmit and M_R receive antennas co-located in a two-dimensional plane.

Assuming that the target lies in the far field (here, far-field refers to a region where the distance from the antennas is much greater than the antenna aperture) of the radar system, the reflected waves received at each antenna element are almost parallel. The phase values of the signals from the ith receiving antenna element, whose horizontal and vertical positions are $x_{R,i}$ and $z_{R,i}$, respectively, become $\frac{2\pi}{\lambda}\left(z_{R,i}\sin\theta_k + x_{R,i}\cos\theta_k\sin\phi_k\right)$, where $\theta_k \in [-\pi/2, \pi/2]$ and $\phi_k \in [-\pi/2, \pi/2]$ are the elevation and azimuth angles between the radar and the kth target, respectively. In addition, λ is the wavelength corresponding to the centre frequency of the FMCW radar signal. For example, $(\theta_k, \phi_k) = (0, 0)$ means that the kth target is exactly in the normal direction of the antenna array plane. The phase of each receive antenna of signals from the kth target is proportional to the receive-array steering vector $\mathbf{a}_R(\theta_k, \phi_k) \in \mathbb{C}^{M_R}$ expressed as follows:

$$\mathbf{a}_R(\theta_k, \phi_k)_{[i]} = \frac{1}{\sqrt{M_R}}e^{j\frac{2\pi}{\lambda}\left(z_{R,i}\sin\theta_k + x_{R,i}\cos\theta_k\sin\phi_k\right)}. \quad (5)$$
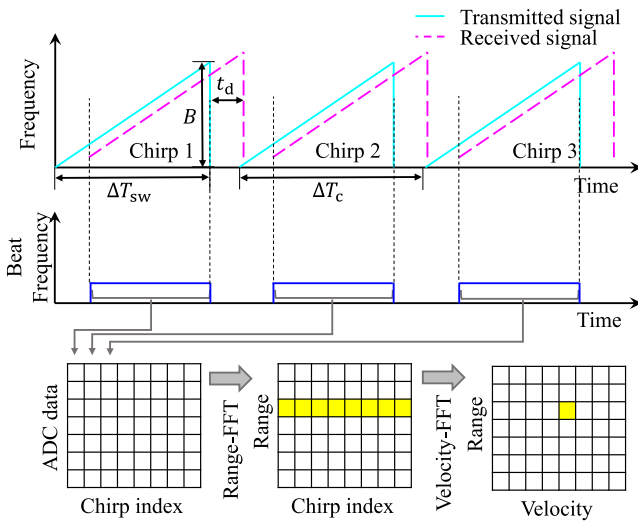

FIGURE 1 Target information (i.e., range and velocity) estimation in the fast-chirp frequency-modulated continuous wave (FMCW) radar system

Using M_T transmit antennas with time-division multiplexing in transmission can generate a maximum of $M_T M_R$ virtual antennas using the MIMO antenna principle [33]. The steering vectors of the MIMO virtual array can be expressed as $\mathbf{a}(\theta_k, \phi_k) = \mathbf{a}_T(\theta_k, \phi_k) \otimes \mathbf{a}_R(\theta_k, \phi_k) \in \mathbb{C}^{M_T M_R}$, where $\mathbf{a}_T(\theta_k, \phi_k) \in \mathbb{C}^{M_T}$ is the transmit-array steering vector. We define the array response using the steering vector of the MIMO virtual array. As shown in Figure 2a, the array response consisting of signals of the same bin on the range-velocity map can be written as follows:

$$\mathbf{y} = \sum_{k=1}^{K} \mathbf{a}(\theta_k, \phi_k)\mathbf{s}_k + \mathbf{w}, \qquad (6)$$

where $\mathbf{s}_k$ denotes the target reflection coefficient for the kth target and the additive noise $\mathbf{w} \in \mathbb{C}^M$ is assumed to be white Gaussian noise. Because obtaining $\mathbf{a}(\theta_k, \phi_k)$ and $\mathbf{s}_k$ directly from Equation (6) is difficult, the following section formulates the problem differently from Equation (6).

3 | INTERPRETATION OF DoA ESTIMATION AS COMPRESSIVE SENSING

3.1 | CS-based DoA estimation in FMCW MIMO radar

This section redefines Equation (6) as a CS problem to obtain the target information from the array response. To this end, the entire DoA FoV is discretised into a fine grid. It is assumed that the possible target azimuth angles comply with a grid of G_A points $\phi_{1:G_A}$, and the elevation angles comply with a grid of G_E points $\theta_{1:G_E}$. Since each azimuth and elevation pair parameterises one steering vector $\mathbf{a}(\theta_p, \phi_q) \in \mathbb{C}^M$, we can define the sensing matrix as $\mathbf{A} = [\mathbf{a}(\theta_1, \phi_1), \mathbf{a}(\theta_1, \phi_2), \dots, \mathbf{a}(\theta_{G_E}, \phi_{G_A})] \in \mathbb{C}^{M \times G_E G_A}$. The array response in Equation (6) can be represented as

$$\mathbf{y} = \mathbf{Ax} + \mathbf{w}. \qquad (7)$$

FMCW MIMO radars can achieve a high range resolution because they offer a wide bandwidth. As a result, only a few targets fall in the same range-velocity bin; the targets are sparse in the DoA estimation x [34]. Mathematically, x is K-sparse when it has at most K nonzero elements, that is, $\|\mathbf{x}\|_0 \leq K$ [35]. The nonzero elements of x lie only on indices corresponding to the DoA at which the target exists. This sparsity can be exploited by CS algorithms for target DoA estimation.

A classic way to recover the K-sparse vector x in Equation (7) is expressed as

$$\hat{\mathbf{x}} = \underset{\mathbf{x}:\|\mathbf{x}\|_0 \leq K}{\arg\min} \|\mathbf{Ax} - \mathbf{y}\|_2^2, \qquad (8)$$
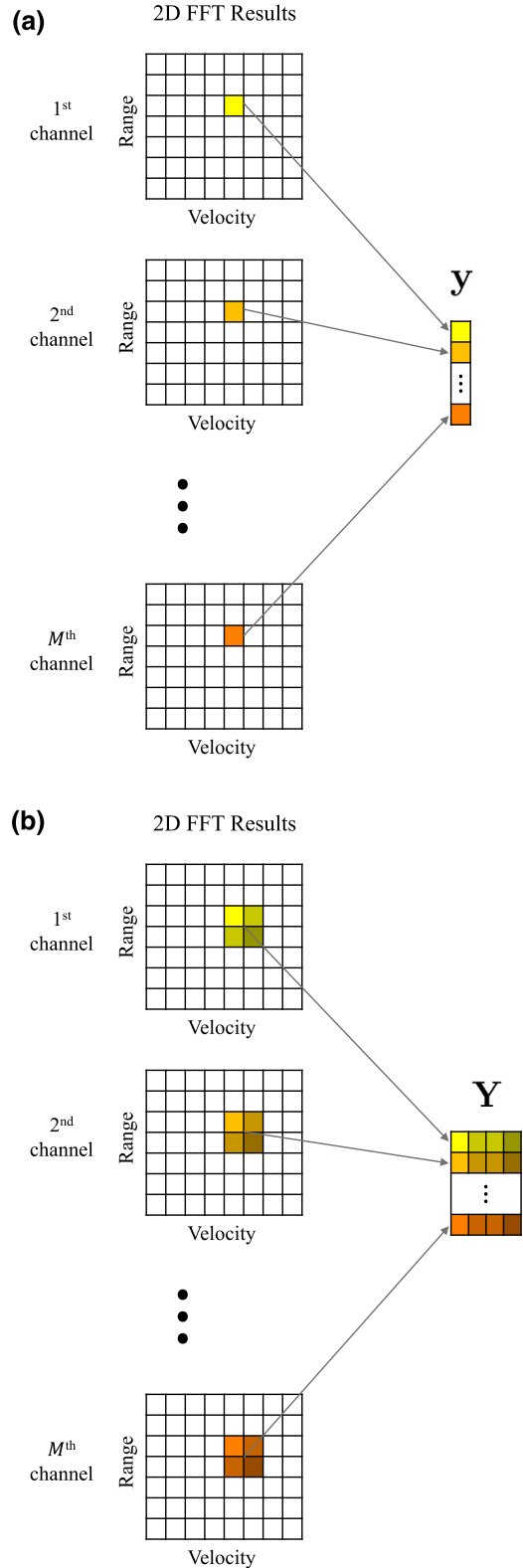

FIGURE 2 Process of generating a vector $\mathbf{y} \in \mathbb{C}^M$ (a) and process of generating a matrix $\mathbf{Y} \in \mathbb{C}^{M \times L}$ (b) from range-velocity maps, which are outputs of 2D FFT. (a) Process of generating $\mathbf{y}$ from the range-velocity maps. (b) Process of generating $\mathbf{Y}$ from the range-velocity maps

and is called subset selection [36–38]. Alternative formulations are

$$\hat{\mathbf{x}} = \arg \min_{\mathbf{x}} \|\mathbf{x}\|_0 \text{ s.t. } \|\mathbf{A}\mathbf{x} - \mathbf{y}\|_2^2 < \epsilon \qquad (9)$$

or

$$\hat{\mathbf{x}} = \arg \min_{\mathbf{x}} \frac{1}{2}\|\mathbf{A}\mathbf{x} - \mathbf{y}\|_2^2 + \lambda \|\mathbf{x}\|_0. \qquad (10)$$

In the field of CS, to ensure the recovery of K-sparse signals with high probability from the above Equations (8–10), the sensing matrix $\mathbf{A}$ is generally assumed to be incoherent [39]. We define the coherence of matrix $\mathbf{A}$ as the largest absolute inner product between any two columns [40, 41], and it is expressed as follows:

$$\mu(\mathbf{A}) = \max_{i \neq j} \frac{\left|\mathbf{A}_{[:,i]}^H \mathbf{A}_{[:,j]}\right|}{\|\mathbf{A}_{[:,i]}\|_2 \|\mathbf{A}_{[:,j]}\|_2}. \qquad (11)$$

Here, $\mathbf{A}$ is incoherent if $\mu(\mathbf{A})$ is small.

To reduce the discretisation error and achieve super-resolution, the FoV should be discretised into a dense grid, that is, G_A and G_E should be large enough. This means that the steering vectors corresponding to the adjacent DoAs have a high correlation, and the sensing matrix $\mathbf{A}$ is coherent. Thus, defining DoA estimation as an SMV CS problem has apparent limitations in achieving super-resolution.

3.2 | Formulation of MMV problem and conventional approaches

As in the previous section, if we try to recover each sparse vector x, in a similar range-velocity bin, x will exhibit similar indices for their nonzero elements. To exploit this joint sparsity among neighbouring range-velocity bins, we stack these all L vectors into the columns of a matrix $\mathbf{Y} \in \mathbb{C}^{M \times L}$. In addition, because the signals are correlated while the noise components are uncorrelated, higher signal-to-noise ratio can be achieved if L range-velocity bins are used together. Figure 2b shows the process of generating $\mathbf{Y}$ where $L = 4$. The goal is to recover $\mathbf{X} \in \mathbb{C}^{G_E G_A \times L}$, which has at most K nonzero rows, that is, $|\text{supp}(\mathbf{X})| < K$. This problem is referred to as the MMV problem. The array response in MMV form is expressed as

$$\mathbf{Y} = \mathbf{A}\mathbf{X} + \mathbf{W}, \qquad (12)$$

where the additive noise $\mathbf{W} \in \mathbb{C}^{M \times L}$ is assumed to be the white Gaussian noise.

Subspace-based methods such as MUSIC [16] and ESPRIT [17–20] can achieve super-resolution in this MMV problem. Subspace-based methods assume that $\mathbf{X}$ has K nonzero rows. They use the property that the dominant K-dimensional eigenspace of the covariance matrix (i.e., $\mathbf{R_Y} = \frac{1}{L}\mathbf{Y}\mathbf{Y}^H$) consists

of steering vectors corresponding to the target. However, subspace-based methods have practical limitations to be used in DoA estimation in FMCW MIMO radars. They commonly require the assumption that $|\text{supp}(\mathbf{X})| = K$. Subspace-based methods provide guaranteed recovery where the assumption $|\text{supp}(\mathbf{X})| = K$ is correct; otherwise, they suffer from performance degradation. Unfortunately, the number of targets in specific range-velocity bins, that is, $|\text{supp}(\mathbf{X})|$, is hardly known to FMCW MIMO radars. Another disadvantage of subspace-based methods is their high computational complexity. These methods need to perform eigenvalue decomposition of $\mathbf{Y}^H\mathbf{Y}$, which requires the computational complexity of $\mathcal{O}(M^3)$ floating-point operations [21]. Therefore, algorithms that are faster than subspace-based methods and do not require information on the number of targets are needed.

Greedy methods are another primary approach for solving MMV problems. Most of them, including simultaneous orthogonal matching pursuit (SOMP) [42], are natural extensions of the SMV problem [43–47], but some are designed solely for the MMV setting [48]. SOMP, one of the most representative and intuitive greedy methods, is outlined in Algorithm 1.

Algorithm 1 SOMP

Input: $\mathbf{Y}$
Output: $\mathbf{X}^{(T)}$
$\mathbf{R}^{(0)} = \mathbf{Y}, S^{(0)} = \emptyset, \mathbf{X}^{(T)} = \mathbf{0}$
for $(t = 0; t < T; t \leftarrow t + 1)$ **do**

$\quad j^{(t+1)} = \arg \min_j \left\| \left(\mathbf{R}^{(t)^H}\mathbf{A}\right)_{[:,j]} \right\|_1$

$\quad S^{(t+1)} = S^{(t)} \cup \left\{ j^{(t+1)} \right\}$

$\quad \mathbf{R}^{(t+1)} = \mathbf{Y} - \mathbf{A}_{[:,S^{(t+1)}]} \mathbf{A}_{[:,S^{(t+1)}]}^\dagger \mathbf{Y}$

end
$\mathbf{X}_{[S^{(T)},:]}^{(T)} = \mathbf{A}_{[:,S^{(T)}]}^\dagger \mathbf{Y}$
return $\underline{\mathbf{X}^{(T)}}$

Greedy methods aim to solve the analogues of (8), (9), or (10) in the MMV case, expressed as follows:

$$\hat{\mathbf{X}} = \arg \min_{\mathbf{X}:|\text{supp}(\mathbf{X})| \leq K} \|\mathbf{A}\mathbf{X} - \mathbf{Y}\|_F^2, \qquad (13)$$

$$\hat{\mathbf{X}} = \arg \min_{\mathbf{X}} |\text{supp}(\mathbf{X})| \text{ s.t. } \|\mathbf{A}\mathbf{X} - \mathbf{Y}\|_F^2 < \epsilon, \qquad (14)$$

or

$$\hat{\mathbf{X}} = \arg \min_{\mathbf{X}} \frac{1}{2}\|\mathbf{A}\mathbf{X} - \mathbf{Y}\|_F^2 + \lambda |\text{supp}(\mathbf{X})|, \qquad (15)$$

respectively. However, because function $|\text{supp}(\mathbf{X})|$ is nonconvex, Equations (13)–(15) are NP-hard problems [49]. This fact suggests that greedy methods cannot guarantee fast computation and good accuracy simultaneously.

To obtain accurate solutions with numerical optimality guarantees, we use the convex relaxation approach. In the MMV case, convex relaxation replaces $|\text{supp}(\cdot)|$ with its convex approximation $\|\cdot\|_{p,1}$, where the mixed $l_{p,q}$ norms for matrices are defined as

$$\|\mathbf{X}\|_{p,q} = \left(\sum_i \|\mathbf{X}_{[i,:]}\|_p^q \right)^{1/q} \qquad (16)$$

for some $q > 1$. In Equation (16), the typical value of q is 2 [50–55], and this optimisation model has been applied in dynamic MRI [56], gene finding [57–59], and many other fields [31, 60]. Specifically, the convex relaxation form of Equation (10) is called the group lasso [31], which is expressed as

$$\hat{\mathbf{X}} = \arg\min_{\mathbf{X}} \frac{1}{2}\|\mathbf{AX} - \mathbf{Y}\|_F^2 + \lambda\|\mathbf{X}\|_{2,1}. \qquad (17)$$

Multi-vectors focal undetermined system solver (MFO-CUSS) [51] is the first algorithm to address the group lasso problem. MFOCUSS can be understood as an iterative reweighted least squares algorithm. As in the least squares algorithm, MFOCUSS computes the inverse of size $M \times M$ matrix at every iteration; hence is computationally expensive for this problem. In the next section, we propose a more efficient algorithm for the group lasso and apply it to the DoA estimation problem in the FMCW MIMO radar.

4 | PROPOSED CS-BASED DoA ESTIMATION IN FMCW MIMO RADAR

4.1 | Basic concept of ISTA

One popular approach that can reduce the computational time required to solve the group lasso (17) is to apply the proximal-gradient method. Specifically, ISTA involves finding proximal mapping associated with the regulariser $\lambda\|\mathbf{X}\|_{2,1}$. The proximal mapping associated with $\lambda\|\cdot\|_{2,1}$ can be computed analytically as follows:

$$\text{prox}_{\lambda\|\cdot\|_{2,1}}(\mathbf{X}) = \arg\min_{\mathbf{U}} \left\{ \frac{1}{2}\|\mathbf{U} - \mathbf{X}\|_F^2 + \lambda\|\mathbf{U}\|_{2,1} \right\} = \mathcal{T}_\lambda(\mathbf{X}), \qquad (18)$$

where operator $\mathcal{T}_\alpha(\cdot)$ is the soft-thresholding operator, which is defined as

$$\mathcal{T}_\alpha(\mathbf{X})_{[i,:]} = \max\left(0, 1 - \frac{\alpha}{\|\mathbf{X}_{[i,:]}\|_2}\right)\mathbf{X}_{[i,:]}. \qquad (19)$$

In each iteration, the proximal mapping (18) is applied to the gradient of the first term of (17), which can be expressed as

$$g(\mathbf{X}) = \frac{d}{d\mathbf{X}}\frac{1}{2}\|\mathbf{AX} - \mathbf{Y}\|_F^2 = \mathbf{A}^H(\mathbf{AX} - \mathbf{Y}). \qquad (20)$$

Thus, the iterative step of ISTA applied to the group lasso (17) is given by

$$\mathbf{X}^{(t+1)} = \text{prox}_{\lambda\|\cdot\|_{2,1}}\left(\mathbf{X}^{(t)} - \frac{1}{L_f}g\left(\mathbf{X}^{(t)}\right) \right)$$
$$= \mathcal{T}_{\lambda/L_f}\left(\left(\mathbf{I}_{M\times M} - \frac{1}{L_f}\mathbf{A}^H\mathbf{A} \right)\mathbf{X}^{(t)} + \frac{1}{L_f}\mathbf{A}^H\mathbf{Y} \right), \qquad (21)$$

where L_f is the greatest eigenvalue of $\mathbf{A}^H\mathbf{A}$. The ISTA for solving (17) is summarised in Algorithm 2.

Algorithm 2 ISTA for solving (17)

Input: $\mathbf{Y}$
Output: $\mathbf{X}^{(T)}$
$\mathbf{X}^{(0)} = \mathbf{A}^H\mathbf{Y}$
for $(t = 0; t < T; t \leftarrow t + 1)$ **do**
　　$\mathbf{X}^{(t+1)} = \mathcal{T}_{\lambda/L_f}\left(\left(\mathbf{I} - \frac{1}{L_f}\mathbf{A}^H\mathbf{A} \right)\mathbf{X}^{(t)} + \frac{1}{L_f}\mathbf{A}^H\mathbf{Y} \right)$
end
return $\underline{\mathbf{X}^{(T)}}$

As in Equation (21), ISTA performs matrix multiplication and soft-thresholding in each iteration. Operations in ISTA have lower computational complexity than the eigenvalue decomposition in MUSIC or the inverse operation in MFO-CUSS. Thus, it is likely that ISTA has less computational time than algorithms such as MUSIC and MFOCUSS. However, because ISTA is iterative, computational time increases proportionally to the number of iterations. In the worst possible case, ISTA converges at a rate of $\mathcal{O}(1/t)$ (i.e., the difference of the objective function values between the tth iteration and an optimal solution point is inversely proportional to t) [30], which is quite slow and requires many iterations.

One method to achieve faster convergence and fewer iterations is to use algorithms that have momentum. A study [30] proposed an acceleration scheme to reduce the number of iterations, which improved the convergence rate of gradient descent from $\mathcal{O}(1/t)$ to $\mathcal{O}(1/t^2)$. The application of Ref. [30] to ISTA is referred to as FISTA [61]. One standard momentum parameter for FISTA is $\beta^{(t)} = \frac{t-1}{t+2}$ [62]. The FISTA for solving (17) is summarised in Algorithm 3.

Algorithm 3 FISTA for solving (17)

Input: $\mathbf{Y}$
Output: $\mathbf{X}^{(T)}$
$\mathbf{X}^{(0)} = \mathbf{A}^H\mathbf{Y}$
for $(t = 0; t < T; t \leftarrow t + 1)$ **do**
　　$\mathbf{Z}^{(t+1)} = \mathcal{T}_{\lambda/L_f}\left(\left(\mathbf{I} - \frac{1}{L_f}\mathbf{A}^H\mathbf{A} \right)\mathbf{X}^{(t)} + \frac{1}{L_f}\mathbf{A}^H\mathbf{Y} \right)$

　　$\beta^{(t+1)} = t/(t+3)$
　　$\mathbf{X}^{(t+1)} = \mathbf{Z}^{(t+1)} + \beta^{(t+1)}(\mathbf{Z}^{(t+1)} - \mathbf{Z}^{(t)})$
end
return $\underline{\mathbf{X}^{(T)}}$

However, ISTA and FISTA only consider the case in which the group lasso is solved for one input. To solve the lasso problem for many inputs, a seminal work [63], named LISTA, proposed training a neural network whose input is $\mathbf{Y}$ and output is $\hat{\mathbf{X}}$ in Equation (17). LISTA considers iterative algorithms as a recurrent neural network, where the tth iteration is regarded as the tth layer in a network. LISTA shows better performance than ISTA/FISTA on new inputs for the same number of iterations (i.e., layers). Many studies over the few years have used LISTA's concepts to solve the (group) lasso [29, 64–70]. We extend SLISTA [29], the study for solving the lasso, to the group lasso and use it for DoA estimation.

Extended SLISTA has two advantages when applied to DoA estimation in the FMCW MIMO radar. The first advantage of SLISTA is that the network learns parameters in an unsupervised manner. Supervised learning is not feasible because we only know the measurement $\mathbf{Y}$, not the ground truth $\mathbf{X}$. The second advantage of SLISTA is that the network has extremely few learnable parameters. For DoA estimation in FMCW MIMO radar problems, the sensing matrix $\mathbf{A}$ has a large size. LISTA and other works have many learnable parameters above the size of $\mathbf{A}$ (i.e., $MG_{\mathrm{E}}G_{\mathrm{A}}$), making network learning difficult. SLISTA, on the other hand, learns only step sizes $\{\alpha^{(t)}\}_{t=1}^{T}$, so the number of learnable parameters is equal to that of iterations (i.e., layers) T. SLISTA for solving (17) is summarised in Algorithm 4.

Algorithm 4 SLISTA for solving (17)

Input: $\mathbf{Y}$
Output: $\mathbf{X}^{(T)}$
$\mathbf{X}^{(0)} = \mathbf{A}^H \mathbf{Y}$
for $(t = 0; t < T; t \leftarrow t + 1)$ **do**
 $\mathbf{X}^{(t+1)} = $
  $\mathcal{T}_{\alpha^{(t+1)}\lambda}\left(\left(\mathbf{I} - \alpha^{(t+1)}\mathbf{A}^H\mathbf{A}\right)\mathbf{X}^{(t)} + \alpha^{(t+1)}\mathbf{A}^H\mathbf{Y}\right)$
end
return $\underline{\mathbf{X}^{(T)}}$

4.2 | Proposed SLISTA-based fast DoA estimation

In this section, we explain how to extend SLISTA to the group lasso to solve the DoA estimation problem in FMCW MIMO radar. In our application, the recovered matrix $\mathbf{X}$ represents four-dimensional (range-velocity-azimuth-elevation) data. Each column in $\mathbf{X}$ represents a sparse vector in $\mathbb{C}^{G_{\mathrm{A}}G_{\mathrm{E}}}$ containing azimuth-elevation information of targets corresponding to one range-velocity bin. To make the network input $\mathbf{Y}$, we crop the 2D-FFT output of size $N_{\mathrm{ADC}} \times N_c \times M$ into $W_R \times W_D \times M$, where W_R and W_D are window sizes along the range and velocity axes, respectively. Then $\mathbf{Y}$ is reshaped into $\mathbb{C}^{M \times W_R W_D}$; hence $\mathbf{X} \in \mathbb{C}^{G_{\mathrm{A}}G_{\mathrm{E}} \times W_R W_D}$.

Before optimising Equation (17), the objective function of ISTA/FISTA/SLISTA, we must normalise input $\mathbf{Y}$. Consider the problem of optimising only the first term of Equation (17) as follows:

$$\hat{\mathbf{X}} = \arg\min_{\mathbf{X}} \frac{1}{2}\|\mathbf{A}\mathbf{X} - \mathbf{Y}\|_F^2. \tag{22}$$

If we take $\gamma\mathbf{Y}$ instead of $\mathbf{Y}$ as input of Equation (22) for an arbitrary nonzero constant $\gamma \in \mathbb{C}$, the output will be $\gamma\hat{\mathbf{X}}$. In this case, we can always recover $\mathbf{X}$ through normalisation, hence normalising $\mathbf{Y}$ before optimisation is unnecessary. However, in Equation (17), the first and second terms differ in the exponent; the first is quadratic, but the second is linear. Because of the difference in exponent between the two terms, the output will not be $\gamma\hat{\mathbf{X}}$ when we take $\gamma\mathbf{Y}$ as the input of Equation (17). This fact suggests that $\mathbf{X}$ can be recovered entirely differently depending on the magnitude of $\mathbf{Y}$, which varies exponentially depending on the measurement environment. Therefore, for robust DoA estimation, the input scale of ISTA/FISTA/SLISTA must all be similar, that is, $\mathbf{Y}$ should be normalised before applying DoA estimation algorithms.

We normalise $\mathbf{Y}$ so that $\|\mathbf{Y}\|_{\max} = 1$, where the maximum norm is defined as $\|\mathbf{Y}\|_{\max} = \max_{ij}|\mathbf{Y}_{[i,j]}|$. Let the notation $\tilde{\mathbf{Y}}$ denote the matrix before normalisation and $\mathbf{Y}$ denote the matrix after normalisation. The relation between $\tilde{\mathbf{Y}}$ and $\mathbf{Y}$ is expressed as follows:

$$\mathbf{Y} = \frac{1}{\|\tilde{\mathbf{Y}}\|_{\max}}\tilde{\mathbf{Y}}. \tag{23}$$

If $\mathbf{X}$ is recovered from the normalised matrix $\mathbf{Y}$, $\mathbf{X}$ has no information about the original signal magnitude. To reconstruct the signal magnitude, the recovered matrix must have a scale of $\tilde{\mathbf{Y}}$. Thus, the recovered matrix which has signal strength information $\tilde{\mathbf{X}}$ is obtained as $\tilde{\mathbf{X}} = \|\tilde{\mathbf{Y}}\|_{\max}\mathbf{X}$.

We train SLISTA using back-propagation in an unsupervised manner. The network learns to solve the group lasso from the experimental dataset $\{\mathbf{Y}_i\}_{i=1}^{N_{\mathrm{train}}}$, where N_{train} represents the number of training samples. The loss function is the sum of the objective function in Equation (17), which is expressed as

$$\mathcal{L}(\Theta) = \sum_{i=1}^{N_{\mathrm{train}}}\left[\frac{1}{2}\|\mathbf{A}f(\mathbf{Y}_i; \Theta) - \mathbf{Y}_i\|_F^2 + \lambda\|f(\mathbf{Y}_i; \Theta)\|_{2,1}\right], \tag{24}$$

where $f(\mathbf{Y}; \Theta)$ is the sparse output of the SLISTA network with learnable parameters $\Theta = \{\alpha^{(1)}, ..., \alpha^{(T)}\}$.

Figure 3 shows the process using SLISTA as the DoA estimation algorithm. Because other algorithms, such as ISTA/FISTA/MFOCUSS, do not have learnable parameters, $f(\mathbf{Y}_i; \Theta)$ should be changed to $f(\mathbf{Y}_i)$ for those cases. Where MUSIC is employed as the DoA estimation algorithm, normalisation is not required; hence the normalisation process in Figure 3 should be eliminated.
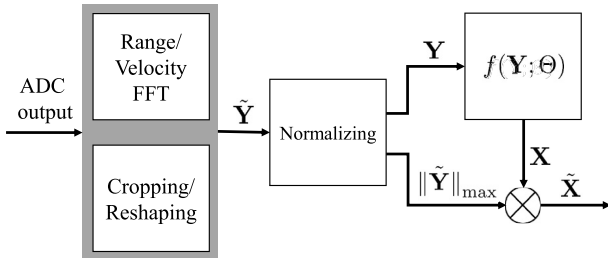
FIGURE 3 Block diagram of the proposed DoA estimation process with normalisation. The input is the ADC output (i.e., $b[m, n]$), and the output is the DoA estimation result (i.e., $\widehat{\mathbf{X}}$). The network $f(\mathbf{Y}_i; \Theta)$ is trained with examples from the experimental dataset

FIGURE 4 Positions of $M = 134$ virtual array elements in the multiple-input multiple-output (MIMO) antenna system

TABLE 1 Specifications of the multiple-input multiple-output (MIMO) radar

Parameters	Values
Centre frequency, f_c	78.3 GHz
Bandwidth, B	2.53 GHz
Sweep slope, S	79.0 MHz/μs
Chirp period, ΔT_c	46 μs
Sampling period, ΔT_s	0.125 μs
The number of transmit antennas, M_T	12
The number of receive antennas, M_R	16
The number of non-duplicated antennas, M	134
The number of chirps, N_C	64
The number of ADC samples, N_{ADC}	256
Size of range bin, Δr	5.93 cm
Size of velocity bin, Δv	5.42 cm/s

5 | EXPERIMENTAL RESULTS

5.1 | Measurement environment

In our experiments, we used the fast-chirp FMCW MIMO radar system, AWR2243 cascade [11], developed by Texas Instruments. This radar uses 78.3 GHz as the centre frequency and 2.53 GHz as the bandwidth. The number of transmit antennas and receive antennas is 12 and 16, respectively, forming a total of 192 (i.e., $M_T M_R = 192$) virtual antennas according to the MIMO principle. Because some MIMO virtual array elements are duplicated in the same location, we only used 134 virtual antennas (i.e., $M = 134$), excluding overlapped 58 cases. The positions of the MIMO virtual array elements are shown in Figure 4. In addition, a total of 64 chirps were used, and 256 ADC samples were obtained from each chirp. Table 1 summarises the specifications of the radar system we used.

We define grid points in the azimuth and elevation directions as explained in Section 3. As shown in the MIMO virtual array in Figure 4, the horizontal (i.e., in x-axis) and vertical (i.e., in z-axis) apertures are 85 and 6 times the half wavelength, respectively. Suppose the angle-FFT is applied in a uniform linear array, whose aperture is 85 times the half-wavelength. In that case, the grid size G_A is 86, and sine values $\sin \phi_{1:86}$ are equidistant, that is, $\phi_p = \arcsin(-1 + 2p/86)$. Similarly, we obtain $\theta_q = \arcsin(-1 + 2q/7)$. To achieve super-resolution, we made the grids finer than in this case. Considering that the beam pattern of the antenna does not cover all DoAs, we took $\sin \phi_p \in [-0.8, 0.8]$ and $\sin \theta_q \in [-0.5, 0.5]$. Moreover, we set G_A and G_E to 128 and 8, which are greater than 86 and 7, respectively. The grid points for achieving super-resolution are defined as

$$\phi_p = \arcsin\left(-0.8 + \frac{1.6}{128}p\right), \quad (p \leq 128, p \in \mathbb{N}), \quad (25)$$

and

$$\theta_q = \arcsin\left(-0.5 + \frac{1.0}{8}q\right), \quad (q \leq 8, q \in \mathbb{N}). \quad (26)$$

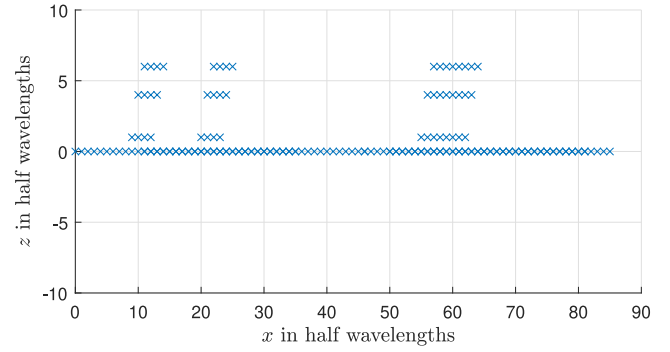Our purpose is to train the network to optimise the loss function (24), but only a few range-velocity bins correspond to the actual target (i.e., most of the range-velocity bins correspond to the empty space); hence, a small number of $\widehat{\mathbf{Y}}$s are appropriate for training. Therefore, we created a training set with only $\widehat{\mathbf{Y}}$s where the radar target existed. As this approach reduces the amount of data, we use data augmentation to avoid overfitting.

First, we normalised and applied FISTA to $\widehat{\mathbf{Y}}$s obtained by the experiment. Among the output $\widehat{\mathbf{X}}$s $\left(\widehat{\mathbf{X}} \in \mathbb{C}^{G_A G_E \times L}\right)$, the signals corresponding to the actual target are nonzero rows. Because the l_2-norm of nonzero rows represents the signal strength from corresponding DoAs, we collected 100 nonzero rows with the largest l_2-norm of $\widehat{\mathbf{X}}$s. Then, we created virtual ground truths (i.e., $\widehat{\mathbf{X}}$s) by rearranging those nonzero rows. In other words, we randomly selected one to five of the 100 rows and placed them in random rows of a zero matrix. Finally, $\mathbf{Y}$ for unsupervised learning was obtained by multiplying the virtual $\mathbf{X}$ and $\mathbf{A}$. By repeating this process 100 times for each number of targets, we got $N_{train} = 500$. SLISTA was trained using the RMSprop optimiser [71] with a learning rate of 10^{-4} for five epochs, until the loss function (24) converged.

We implemented all our algorithms in Python 3.7.6, using the PyTorch 1.9.0 package. These algorithms were performed on a graphic processing unit, NVIDIA RTX 2070 SUPER. When executing MUSIC with $|\text{supp}(\mathbf{X})| = 3$ in this environment, the average execution time for each input $\mathbf{Y} \in \mathbb{C}^{134 \times 16}$ was 11.31 ms. We found that ISTA/FISTA/SLISTA took a shorter execution time than MUSIC when the iteration number T was less than 6, so we set $T = 4$. We also set $\lambda = 5$.
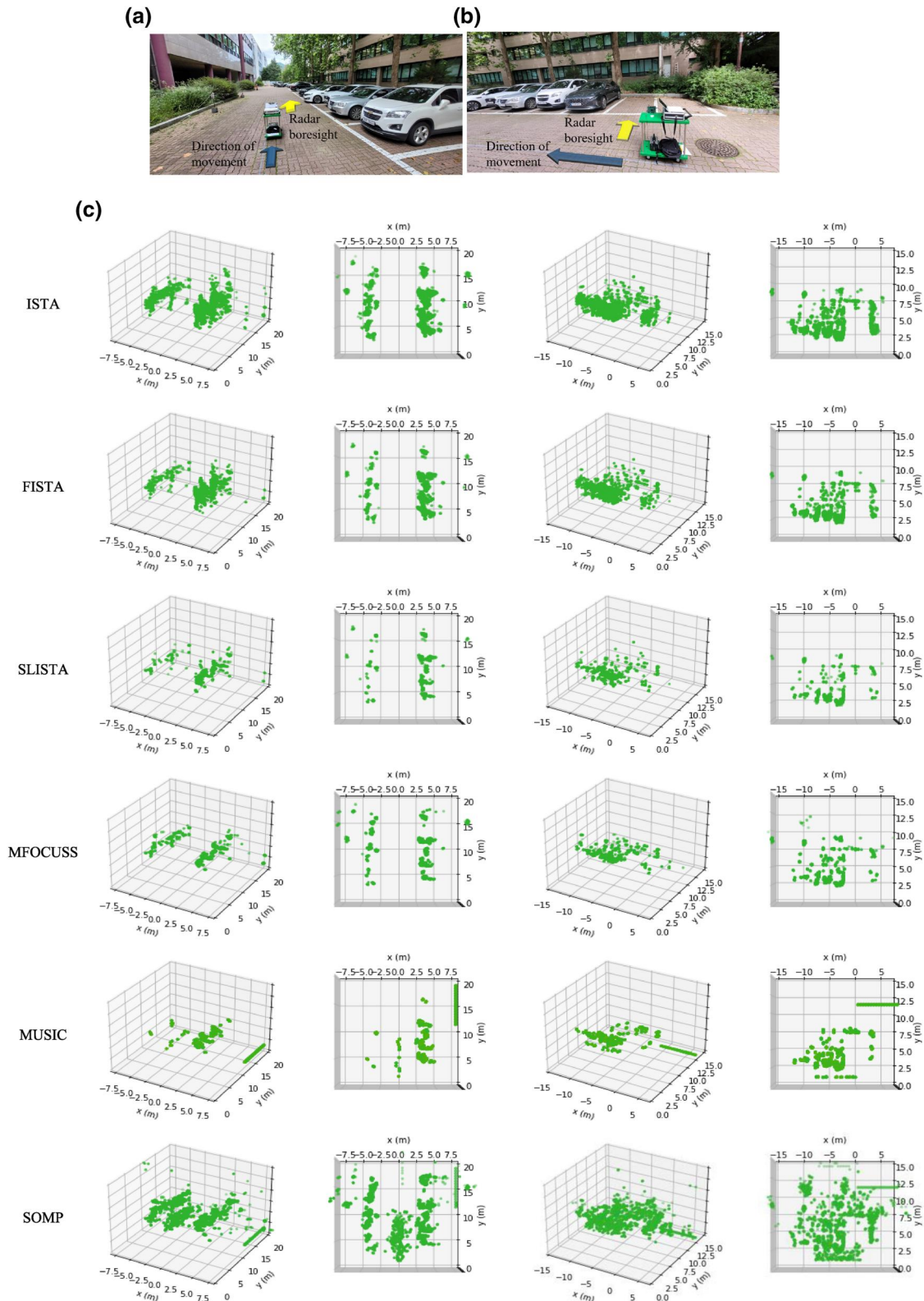

FIGURE 5 Experimental scenarios in the parking lot when the direction of movement and the boresight of the radar are parallel (a), perpendicular (b), and the point cloud generation results (c). The left half of (c) is the result in environment (a), and the right half of (c) is the result in environment (b)

Using this radar system, radar signal measurements were conducted in two different environments. In the first environment, we measured radar signals in a parking lot with cars, as shown in Figure 5a,b. The data were collected with the radar changing its position 16 times by 0.5 m increments along a straight line. Figure 5a shows a scenario in which the direction of the radar movement is parallel to the radar's boresight, and Figure 5b shows a scenario in which they are perpendicular. In the second environment, we measured signals of three corner reflectors at a similar range, as shown in Figure 6. In the following section, we compare the performance of the algorithms by synthesising images generated from the data measured at each location.

5.2 | DoA estimation results

5.2.1 | Experiment in the parking lot

To evaluate the performance of the proposed method, we visualised the detected point clouds for the parking lot, as shown in Figure 5c. As shown in the figure, ISTA and FISTA have poorer elevation estimation accuracy than SLISTA or MFOCUSS. From the top view, we can observe that SLISTA and MFOCUSS are more precise than ISTA or FISTA at the edges of parked cars. Therefore, SLISTA also exhibits good imaging performance for actual targets on the road. To compare with the proposed method, we implemented MUSIC and SOMP on the data for the parking lot scenario, as shown in Figure 5c. MUSIC does not recover $\mathbf{X}$, as in SOMP, but only the nonzero indices of $\mathbf{X}$. We assume that all nonzero values of $\mathbf{X}$ recovered to MUSIC have the same value. As shown in Figure 5c, MUSIC and SOMP detected more targets than actually existed. Thus, we set the support of $\mathbf{X}$, the input required for MUSIC and SOMP, to 1 (i.e., supp($\mathbf{X}$) = 1 in

MUSIC and $T = 1$ in SOMP). Note that each point in SOMP is imaged in the same size scale as in ISTA/FISTA/SLISTA/MFOCUSS.

In Figure 5c, MUSIC and SOMP both imaged targets that did not exist. According to the photographs and imaging results of ISTA/FISTA/SLISTA/MFOCUSS, parking lots should have no targets other than cars and walls. However, MUSIC and SOMP have formed points in many places where there are no targets, including just in front of the radar's boresight. These false detections can be a severe problem when generating radar point clouds for autonomous driving. This problem occurs because both MUSIC and SOMP assume that supp($\mathbf{X}$) = 1. Even if the target does not exist (i.e., $\mathbf{X} = \mathbf{0}$), MUSIC and SOMP generated false detections due to interference and noise. On the other hand, because the methods of solving the group lasso (i.e., ISTA/FISTA/SLISTA/MFOCUSS) do not require information about support and their objective functions have regularisation terms, they form points only where actual targets exist.

5.2.2 | Experiment with corner reflectors

In this section, we analyse the performance of the algorithms in the following aspects. First, we measured the execution time of the algorithms, from obtaining $\tilde{\mathbf{Y}}$ to generating $\tilde{\mathbf{X}}$. The average execution time for ISTA/FISTA/SLISTA/MFOCUSS is shown in the bottom line of Table 2. Second, in a corner reflector measurement experiment, we evaluated how sharply the corner reflector is imaged. Radar-imaged corner reflector should theoretically have only one range and DoA [72], which implies that most nonzero values are concentrated in considerably few indices of $\tilde{\mathbf{X}}$. To evaluate the sharpness, we calculated the ratio of the Frobenius norm to the $l_{1,1}$-norm of $\tilde{\mathbf{X}}$, that is, $\|\tilde{\mathbf{X}}\|_F / \|\tilde{\mathbf{X}}\|_{1,1}$. A high ratio implies that the corner reflectors are sharply imaged. Because corner reflectors were imaged in range bins 141–144 (i.e., 8.36–8.54 m), and 145–148 (i.e., 8.60–8.78 m), we calculated $\|\tilde{\mathbf{X}}\|_F / \|\tilde{\mathbf{X}}\|_{1,1}$ in both ranges. These ratios are shown in Table 2. The execution time section of Table 2 shows that ISTA, FISTA, and SLISTA have less than 11.32 ms of MUSIC. By comparison, we can observe that MFOCUSS has a quite large execution time compared to MUSIC. In terms of sharpness (i.e., $\|\tilde{\mathbf{X}}\|_F / \|\tilde{\mathbf{X}}\|_{1,1}$), SLISTA shows better accuracy than ISTA or FISTA, and worse accuracy than MFOCUSS. Thus, the proposed algorithm, which applies SLISTA to the group lasso, yields the best imaging results among algorithms that are faster than MUSIC.
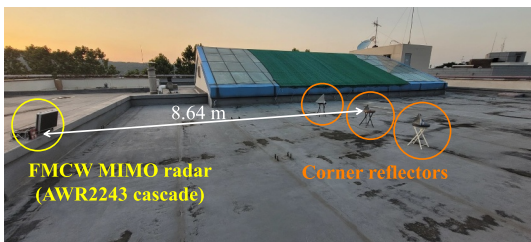

FIGURE 6 Measurement environment with the fast-chirp frequency-modulated continuous wave (FMCW) multiple-input multiple-output (MIMO) radar

T A B L E 2 Direction of arrival (DoA) estimation performance

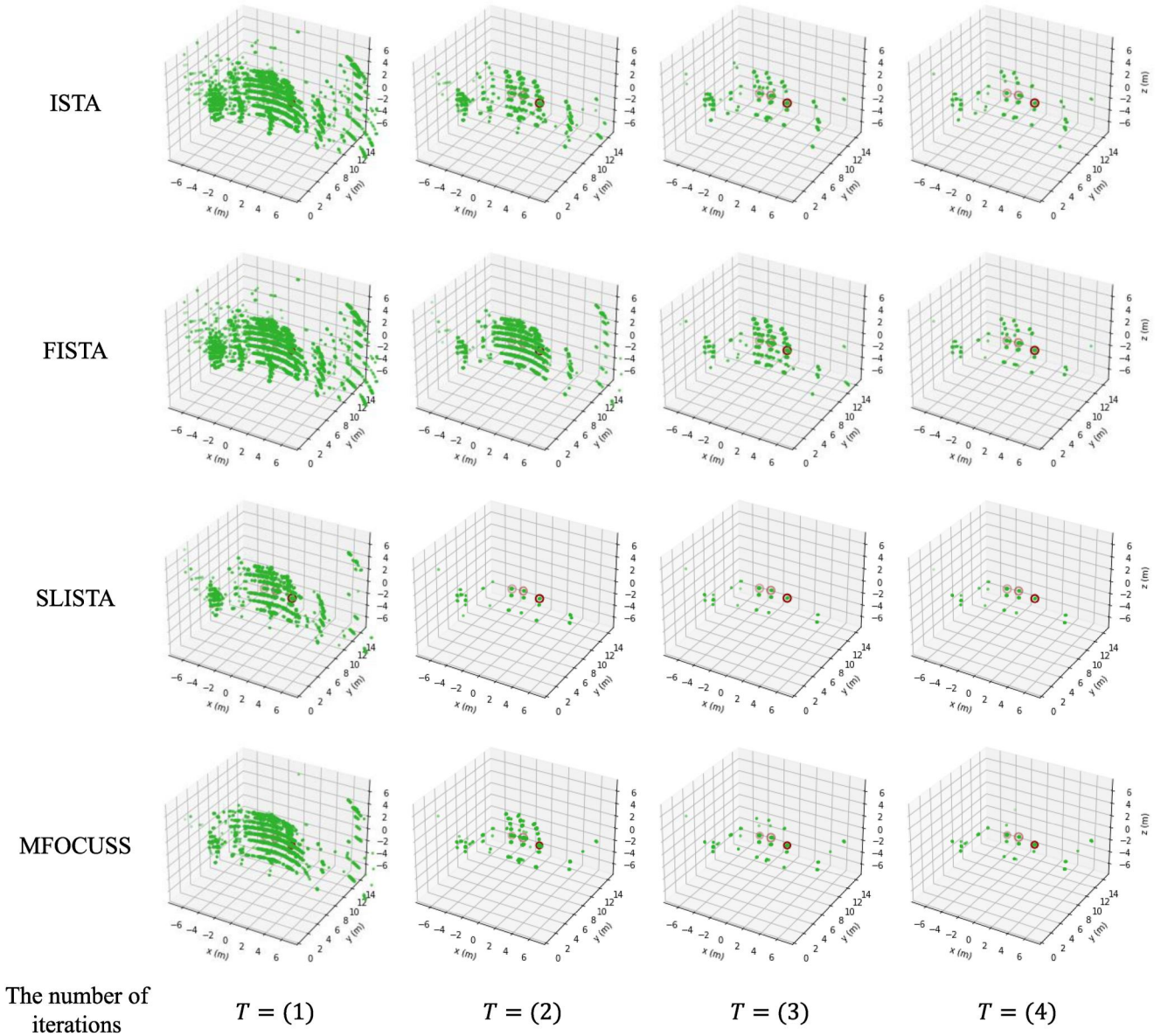|	Range bins (ranges)	ISTA	FISTA	SLISTA	MFOCUSS ($T = 1$)	MFOCUSS ($T = 4$)	MUSIC
$\frac{\|\tilde{\mathbf{X}}\|_F}{\|\tilde{\mathbf{X}}\|_{1,1}}$	141–144 (8.36–8.54 m)	0.190	0.195	0.288	0.080	0.430	N/A
	145–148 (8.60–8.78 m)	0.271	0.261	0.360	0.132	0.503	N/A
Execution time (ms)		7.20	8.08	8.57	11.813	45.5	11.32

FIGURE 7 Point cloud generation results for three corner reflectors. The actual location of the corner reflectors is indicated by red circles

To further analyse the performance of algorithms, we visualised the point clouds for corner reflectors in Figure 7. The actual location of the corner reflectors are indicated by red circles. The size of each point is proportional to the log of the absolute value of each entry of $\mathbf{X}$. Ideally, there should be only three points in the middle, where the actual targets (i.e., three corner reflectors) exist. If the number of iterations is small, many points are imaged where the actual target does not exist. As the number of iterations increased, the point clouds progressively converged into the positions of each corner reflectors. Comparing the number of imaged points at $T = 4$, SLISTA and MFOCUSS showed better DoA estimation performance than ISTA and FISTA. Note that ISTA and FISTA formed many points with an incorrect elevation because of the poor elevation resolution. SLISTA showed better results because the step size was determined considering $T = 4$ and the probabilistic distribution of the target information, whereas ISTA and FISTA did not consider these factors and decided the step size based only on $\mathbf{A}$.

In this section, the performance of the DoA estimation was evaluated using experimental data for each algorithm. We explained that MUSIC and SOMP have the disadvantage of generating false detections compared to the convex relaxation-based methods by comparing the results in Figure 5c. Moreover, Table 2 and Figure 7 show that SLISTA generates the best image with less execution time than MUSIC among methods solving the group lasso (i.e., convex relaxation-based approaches).

6 | CONCLUSION

The main findings of this study can be summarised in two points. First, the DoA estimation for point cloud generation in the FMCW MIMO radar was defined as the group lasso problem. Second, the extended SLISTA for the MMV problem had excellent imaging performance for less computational time than the widely used algorithm, MUSIC. To validate our findings, we collected actual radar data and applied six different DoA estimation algorithms to compare their performances. Experimental results showed that greedy and subspace methods suffered from false detection problems, whereas algorithms solving the group lasso did not. The experimental results also numerically demonstrated that the imaging accuracy of the extended SLISTA outperformed ISTA/FISTA/ MFOCUSS. We expect the proposed method to effectively reduce the time consumed for DoA estimation in the FMCW MIMO radar system.

CONFLICT OF INTEREST

There is no conflict of interest.

DATA AVAILABILITY STATEMENT

Research data are not shared.

ORCID

Seongwook Lee https://orcid.org/0000-0001-9115-4897

REFERENCES

1. Zang, S., et al.: The impact of adverse weather conditions on autonomous vehicles: how rain, snow, fog, and hail affect the performance of a self-driving car. IEEE Veh. Technol. Mag. 14(2), 103–111 (2019). https://doi.org/10.1109/mvt.2019.2892497
2. Chang, K., et al.: A w-band single-chip transceiver for FMCW radar. In: IEEE 1993 Microwave and Millimeter-Wave Monolithic Circuits Symposium Digest of Papers, pp. 41–44. IEEE, Washington (1993)
3. Sun, S., Petropulu, A.P., Poor, H.V.: MIMO radar for advanced driver-assistance systems and autonomous driving: advantages and challenges. IEEE Signal Process. Mag. 37(4), 98–117 (2020). https://doi.org/10.1109/msp.2020.2978507
4. Li, J., Stoica, P.: MIMO radar with colocated antennas. IEEE Signal Process. Mag. 24(5), 106–114 (2007). https://doi.org/10.1109/msp.2007.904812
5. Rao, S.: MIMO radar. Texas Instruments Application Report, pp. 1–12 (2017)
6. Awr1642 single-chip 77- and 79-GHz FMCW radar sensor datasheet (rev. b) (2019)
7. Iwr1642 single-chip 77- and 79-GHz FMCW radar sensor datasheet (rev. b) (2018)
8. 24 GHz radar kit (2tx + 4rx) dk-sr-2400e and sr-2400e: FMCW-radar with ethernet interface (2019)
9. 24 GHz FMCW-radar kit development kit dk-sr-1800e with PC software sentool. (2017)
10. 24 GHz radar kit (1tx + 4rx) dk-sr-14mpc and sr-14mpc: FMCW-radar with can-bus interface (2019)
11. Texas Instruments: AWR2243 Single-Chip 76- to 81-GHz FMCW Transceiver datasheet (Rev. A) (2020)
12. Palffy, A., et al.: CNN based road user detection using the 3D radar cube. IEEE Rob. Autom. Lett. 5(2), 1263–1270 (2020). https://doi.org/10.1109/lra.2020.2967272
13. Gao, X., et al.: Ramp-CNN: a novel neural network for enhanced automotive radar object recognition. IEEE Sensor. J. 21(4), 5119–5132 (2020). https://doi.org/10.1109/jsen.2020.3036047
14. Pérez, R., et al.: Single-frame vulnerable road users classification with a 77 GHz FMCW radar sensor and a convolutional neural network. In: 2018 19th International Radar Symposium (IRS), pp. 1–10. IEEE, Washington (2018)
15. Hong, S., et al.: Radar signal decomposition in steering vector space for multi-target classification. IEEE Sensor. J. 21(22), 25843–25852 (2021). https://doi.org/10.1109/jsen.2021.3116712
16. Schmidt, R.: Multiple emitter location and signal parameter estimation. IEEE Trans. Antenn. Propag. 34(3), 276–280 (1986). https://doi.org/10.1109/tap.1986.1143830
17. Roy, R., Kailath, T.: Esprit-estimation of signal parameters via rotational invariance techniques. IEEE Trans. Acoust. Speech Signal Process. 37(7), 984–995 (1989). https://doi.org/10.1109/29.32276
18. Xu, G., et al.: Beamspace esprit. IEEE Trans. Signal Process. 42(2), 349–356 (1994). https://doi.org/10.1109/78.275607
19. Haardt, M., Nossek, J.A.: Unitary esprit: how to obtain increased estimation accuracy with a reduced computational burden. IEEE Trans. Signal Process. 43(5), 1232–1242 (1995). https://doi.org/10.1109/78.382406
20. Zoltowski, M.D., Haardt, M., Mathews, C.P.: Closed-form 2-d angle estimation with rectangular arrays in element space or beamspace via unitary esprit. IEEE Trans. Signal Process. 44(2), 316–328 (1996). https://doi.org/10.1109/78.485927
21. Jing, X., Du, Z.C.: An improved fast root-music algorithm for DoA estimation. In: 2012 International Conference on Image Analysis and Signal Processing, pp. 1–3. IEEE, Washington (2012)
22. Chen, T., Wu, H., Liu, L.: A joint Doppler frequency shift and DoA estimation algorithm based on sparse representations for colocated TDM-MIMO radar. J. Appl. Math. 1–9 (2014). https://doi.org/10.1155/2014/421391
23. Zheng, C., Chen, H., Wang, A.: High angular resolution for 77 GHz FMCW radar via a sparse weighted quadratic minimization. IEEE Sensor. J. 21(9), 10637–10646 (2021). https://doi.org/10.1109/jsen.2021.3060428
24. Belfiori, F., et al.: Digital beam forming and compressive sensing based DoA estimation in mimo arrays. In: 2011 8th European Radar Conference, pp. 285–288. IEEE, Washington (2011)
25. Chen, L., Bi, D., Pan, J.: Two-dimensional angle estimation of two-parallel nested arrays based on sparse Bayesian estimation. Sensors. 18(10), 3553 (2018). https://doi.org/10.3390/s18103553
26. Ni, Z., Huang, B., Cao, M.: Angular positions estimation of spatially extended targets for MIMO radar using complex spatiotemporal sparse Bayesian learning. IEEE Access. 7, 94473–94480 (2019). https://doi.org/10.1109/access.2019.2926442
27. Chen, J., et al.: Iterative reweighted proximal projection based DoA estimation algorithm for monostatic mimo radar. Signal Process. 172, 107537 (2020). https://doi.org/10.1016/j.sigpro.2020.107537
28. Monga, V., Li, Y., Eldar, Y.C.: Algorithm unrolling: interpretable, efficient deep learning for signal and image processing. IEEE Signal Process. Mag. 38(2), 18–44 (2021). https://doi.org/10.1109/msp.2020.3016905
29. Ablin, P., et al.: Learning step sizes for unfolded sparse coding. Adv. Neural Inf. Process. Syst. 32, 13100–13110 (2019)
30. Bredies, K., Lorenz, D.: Iterative Soft-Thresholding Converges Linearly. Citeseer, Princeton (2007)
31. Yuan, M., Lin, Y.: Model selection and estimation in regression with grouped variables. J. Roy. Stat. Soc. B Stat. Methodol. 68(1), 49–67 (2006). https://doi.org/10.1111/j.1467-9868.2005.00532.x

32. Winkler, V.: Range Doppler detection for automotive FMCW radars. In: 2007 European Radar Conference, pp. 166–169. IEEE, Washington (2007)

33. Friedlander, B.: On the relationship between MIMO and SIMO radars. IEEE Trans. Signal Process. 57(1), 394–398 (2008). https://doi.org/10.1109/tsp.2008.2007106

34. Wang, X., et al.: A sparse representation scheme for angle estimation in monostatic mimo radar. Signal Process. 104, 258–263 (2014). https://doi.org/10.1016/j.sigpro.2014.04.007

35. Eldar, Y.C., Kutyniok, G.: Compressed Sensing: Theory and Applications. Cambridge University Press, Cambridge (2012)

36. Breiman, L.: Better subset regression using the nonnegative garrote. Technometrics. 37(4), 373–384 (1995). https://doi.org/10.1080/00401706.1995.10484371

37. Couvreur, C., Bresler, Y.: On the optimality of the backward greedy algorithm for the subset selection problem. SIAM J. Matrix Anal. Appl. 21(3), 797–808 (2000). https://doi.org/10.1137/s0895479898332928

38. Mallows, C.L.: Some comments on cp. Technometrics. 42(1), 87–94 (2000). https://doi.org/10.1080/00401706.2000.10485984

39. Tropp, J.A.: Greed is good: algorithmic results for sparse approximation. IEEE Trans. Inf. Theor. 50(10), 2231–2242 (2004). https://doi.org/10.1109/tit.2004.834793

40. Donoho, D.L., Elad, M.: Optimally sparse representation in general (nonorthogonal) dictionaries via l_1 minimization. Proc. Natl. Acad. Sci. USA. 100(5), 2197–2202 (2003). https://doi.org/10.1073/pnas.0437847100

41. Tropp, J., et al.: Signal recovery from partial information via orthogonal matching pursuit. IEEE Trans. Inf. Theor. 53(12), 4655–4666 (2007). https://doi.org/10.1109/tit.2007.909108

42. Chen, J., Huo, X.: Sparse representations for multiple measurement vectors (MMV) in an over-complete dictionary. In: Proceedings (ICASSP'05). IEEE International Conference on Acoustics, Speech, and Signal Processing, 2005, vol. 4, pp. iv–257. IEEE, Washington (2005)

43. Foucart, S.: Hard thresholding pursuit: an algorithm for compressive sensing. SIAM J. Numer. Anal. 49(6), 2543–2563 (2011). https://doi.org/10.1137/100806278

44. Blumensath, T., Davies, M.E.: Iterative hard thresholding for compressed sensing. Appl. Comput. Harmon. Anal. 27(3), 265–274 (2009). https://doi.org/10.1016/j.acha.2009.04.002

45. Blumensath, T., Davies, M.E.: Normalized iterative hard thresholding: guaranteed stability and performance. IEEE J. Sel. Topics Signal Process. 4(2), 298–309 (2010). https://doi.org/10.1109/jstsp.2010.2042411

46. Needell, D., Tropp, J.A.: Cosamp: iterative signal recovery from incomplete and inaccurate samples. Appl. Comput. Harmon. Anal. 26(3), 301–321 (2009). https://doi.org/10.1016/j.acha.2008.07.002

47. Blanchard, J.D., et al.: Greedy algorithms for joint sparse recovery. IEEE Trans. Signal Process. 62(7), 1694–1704 (2014). https://doi.org/10.1109/tsp.2014.2301980

48. Tropp, J.A., Gilbert, A.C., Strauss, M.J.: Algorithms for simultaneous sparse approximation. Part I: greedy pursuit. Signal Process. 86(3), 572–588 (2006). https://doi.org/10.1016/j.sigpro.2005.05.030

49. Muthukrishnan, S.: Data streams: Algorithms and Applications. Now Publishers Inc, Delft (2005)

50. Chen, S.S., Donoho, D.L., Saunders, M.A.: Atomic decomposition by basis pursuit. SIAM Rev. 43(1), 129–159 (2001). https://doi.org/10.1137/s003614450037906x

51. Cotter, S.F., et al.: Sparse solutions to linear inverse problems with multiple measurement vectors. IEEE Trans. Signal Process. 53(7), 2477–2488 (2005). https://doi.org/10.1109/tsp.2005.849172

52. Tropp, J.A.: Algorithms for simultaneous sparse approximation. Part II: convex relaxation. Signal Process. 86(3), 589–602 (2006). https://doi.org/10.1016/j.sigpro.2005.05.031

53. Zdunek, R., Cichocki, A.: Improved m-focuss algorithm with overlapping blocks for locally smooth sparse signals. IEEE Trans. Signal Process. 56(10), 4752–4761 (2008). https://doi.org/10.1109/tsp.2008.928160

54. Hyder, M.M., Mahata, K.: A robust algorithm for joint-sparse recovery. IEEE Signal Process. Lett. 16(12), 1091–1094 (2009). https://doi.org/10.1109/lsp.2009.2028107

55. Hu, Y., et al.: Group sparse optimization via lp, q regularization. J. Mach. Learn. Res. 18(1), 960–1011 (2017)

56. Usman, M., et al.: k-t group sparse: a method for accelerating dynamic MRI. Magn. Reson. Med. 66(4), 1163–1176 (2011). https://doi.org/10.1002/mrm.22883

57. Meier, L., Van De Geer, S., Bühlmann, P.: The group lasso for logistic regression. J. Roy. Stat. Soc. B. 70(1), 53–71 (2008). https://doi.org/10.1111/j.1467-9868.2007.00627.x

58. Yang, H., et al.: Online learning for group lasso. In: ICML (2010)

59. Wang, Y., Li, X., Ruiz, R.: Weighted general group lasso for gene selection in cancer classification. IEEE Trans. Cybern. 49(8), 2860–2873 (2018). https://doi.org/10.1109/tcyb.2018.2829811

60. Bach, F.R.: Consistency of the group lasso and multiple kernel learning. J. Mach. Learn. Res. 9(6), 1179–1225 (2008)

61. Beck, A., Teboulle, M.: A fast iterative shrinkage-thresholding algorithm for linear inverse problems. SIAM J. Imag. Sci. 2(1), 183–202 (2009). https://doi.org/10.1137/080716542

62. Taylor, A.B., Hendrickx, J.M., Glineur, F.: Exact worst-case performance of first-order methods for composite convex optimization. SIAM J. Optim. 27(3), 1283–1313 (2017). https://doi.org/10.1137/16m108104x

63. Gregor, K., LeCun, Y.: Learning fast approximations of sparse coding. In: Proceedings of the 27th International Conference on International Conference on Machine Learning, pp. 399–406 (2010)

64. Sprechmann, P., et al.: Supervised sparse analysis and synthesis operators. Adv. Neural Inf. Process. Syst. 26, 908–916 (2013)

65. Giryes, R., et al.: Tradeoffs between convergence speed and reconstruction accuracy in inverse problems. IEEE Trans. Signal Process. 66(7), 1676–1690 (2018). https://doi.org/10.1109/tsp.2018.2791945

66. Yang, Y., et al.: ADMM-net: a deep learning approach for compressive sensing MRI. arXiv preprint arXiv:170506869 (2017)

67. Moreau, T., Bruna, J.: Understanding trainable sparse coding via matrix factorization. arXiv preprint arXiv:160900285 (2016)

68. Chen, X., et al.: Theoretical linear convergence of unfolded ISTA and its practical weights and thresholds. arXiv preprint arXiv:180810038 (2018)

69. Ito, D., Takabe, S., Wadayama, T.: Trainable ISTA for sparse signal recovery. IEEE Trans. Signal Process. 67(12), 3113–3125 (2019). https://doi.org/10.1109/tsp.2019.2912879

70. Liu, J., Chen, X.: ALISTA: Analytic weights are as good as learned weights in LISTA. In: International Conference on Learning Representations (ICLR) (2019)

71. Hinton, G., Srivastava, N., Swersky, K.: Neural networks for machine learning lecture 6A overview of mini-batch gradient descent. Cited on 14(8), 2 (2012)

72. Latmira, G., Sposito, A.: Radar corner reflector for linear or circular polarization. J. Res. NBS D 66, 23–29 (1962)